Multinucleon transfer products in ^{48}Ca, ^{54}Cr+^{243}Am and ^{54}Cr+^{238}U reactions*

G. Xie (谢港)[1,2] Z. Y. Zhang (张志远)[1,2†] J. G. Wang (王建国)[1] L. Ma (马龙)[1,3] M. H. Huang (黄明辉)[1,2,3] C. L. Yang (杨春莉)[1] X. L. Wu (吴晓蕾)[1,3] Z. G. Gan (甘再国)[1,2,3‡] H. B. Yang (杨华彬)[1,2] M. M. Zhang (张明明)[1,2] Y. L. Tian (田玉林)[1,3] Y. S. Wang (王永生)[1,3] J. Y. Wang (王均英)[1,3] Y. H. Qiang (强赟华)[1] L. Zhu (祝霖)[1,2] X. Y. Huang (黄鑫源)[1,2] S. Y. Xu (徐苏扬)[1,2] Z. Zhao (赵圳)[1,2] Z. C. Li (李宗池)[1,2] X. Zhang (张旭)[1,2] H. Zhou (周浩)[1,2] J. H. Zheng (郑佳卉)[1,2] L. C. Sun (孙路冲)[1,4] F. Guan (管芳)[1,5] W. X. Huang (黄文学)[1,2,3] Z. Qin (秦芝)[1,2] Y. Wang (王洋)[1] X. J. Yin (殷小杰)[1] Y. F. Cui (崔云飞)[1,2] Y. He (何源)[1,2] L. T. Sun (孙良亭)[1,2] Z. Z. Ren (任中洲)[6] S. G. Zhou (周善贵)[2,7] V. K. Utyonkov[8] A. A. Voinov[8] Yu. S. Tsyganov[8] A. N. Polyakov[8] D. I. Solovyev[8] D. Ibadullayev[8,9] M. V. Shumeiko[8]

[1]State Key Laboratory of Heavy Ion Science and Technology, Institute of Modern Physics, Chinese Academy of Sciences, Lanzhou 730000, China
[2]School of Nuclear Science and Technology, University of Chinese Academy of Sciences, Beijing 100049, China
[3]Advanced Energy Science and Technology Guangdong Laboratory, Huizhou 516000, China
[4]Shandong Provincial Key Laboratory of Nuclear Science, Nuclear Energy Technology and Comprehensive Utilization, Weihai Frontier Innovation Institute of Nuclear Technology, School of Nuclear Science, Energy and Power Engineering, Shandong University, Shandong 250061, China
[5]Department of Physics, Guangxi Normal University, Guilin 541004, China
[6]School of Physics Science and Engineering, Tongji University, Shanghai 200092, China
[7]CAS Key Laboratory of Theoretical Physics, Institute of Theoretical Physics, Chinese Academy of Sciences, Beijing 100190, China
[8]Joint Institute for Nuclear Research, RU- 141980 Dubna, Russian Federation
[9]Institute of Nuclear Physics, Almaty 050032, Kazakhstan

Abstract: Experiments with ^{48}Ca and ^{54}Cr induced reactions were performed at the gas-filled recoil separator named Spectrometer for Heavy Atoms and Nuclear Structure-2 (SHANS2) of the China Accelerator Facility for superheavy Elements (CAFE2). The isotopic distributions of nuclei produced in the reactions of ^{48}Ca+^{243}Am, ^{54}Cr+^{243}Am, and ^{54}Cr+^{238}U were investigated. Bombardments were conducted at energies near the respective Coulomb barriers, with the SHANS2 magnetic rigidities set to collect fusion-evaporation residues. α-decay spectroscopy was employed to identify products, revealing 58 different isotopes in these experiments. The analysis indicates that the distribution of nuclides produced in different reactions exhibits clear systematic trends. Based on their mass distributions, these nuclei were attributed to the products from the quasi-fission (QF) process. Additionally, several short-lived fission events were identified and attributed to the fission isomers near the target.

Keywords: multinucleon transfer reaction, fission, gas-filled recoil separator, nuclear experiment

DOI: 10.1088/1674-1137/ae4bab **CSTR:** 32044.14.ChinesePhysicsC.50064001

I. INTRODUCTION

Contemporary nuclear physics research endeavors to expand the boundaries of the periodic table and elucidate the fundamental principles governing nuclear stability [1]. The synthesis of superheavy nuclei (SHN) constitutes an important research focus in modern nuclear physics, including rigorous investigations of shell evolution phenomena, structural properties, and the island of stability associated with SHN [2−9]. Although element 118 (Oganesson) currently holds distinction as the heaviest element experimentally confirmed [2], the existence of elements with proton numbers $Z \geq 119$ remains uncon-

Received 15 December 2025; Accepted 2 March 2026; Accepted manuscript online 3 March 2026

* Supported by the Gansu Key Project of Science and Technology (23ZDGA014), the National Key R&D Program of China (2023YFA1606500, 2024YFE0109800, 2024YFE0110400, 2024YFE0110303), the Guangdong Major Project of Basic and Applied Basic Research (2021B0301030006), the National Natural Science Foundation of China (12105328, W2412040, 12475126, 12422507, 12535009, 12375118, 12435008, W2412043), the CAS Project for Young Scientists in Basic Research (YSBR-002), the Youth Innovation Promotion Association of the Chinese Academy of Sciences (2023439), and the Russian Science Foundation (25-42-00003). A. A. V is grateful for the support from CAS President's international Fellowship Initiative (2026PVA0049)

† E-mail: zhangzy@impcas.ac.cn
‡ E-mail: zggan@impcas.ac.cn

firmed and constitutes the next frontier in elemental discovery [10, 11]. This research domain presents significant technical challenges in nuclear synthesis and detection methodologies while offering opportunities for breakthrough discoveries in nuclear structure physics [11−13].

Projectile fragmentation, fission, and fusion reactions serve as versatile tools for producing new nuclei in laboratories. For the synthesis of SHN, fusion reaction is currently the conventional approach. However, model calculations indicate that multinucleon transfer (MNT) reactions at energies near the Coulomb barrier exhibit larger cross-sections for the production of isotopes of elements up to Z ~ 108 [14−16]. Experimental studies have demonstrated that MNT reactions are more efficient owing to their broad excitation functions, which allow for the simultaneous production of different isotopes under the same experimental conditions, whereas fusion reactions only yield a limited number of isotopes. MNT occurs in deep-inelastic collision reactions at energies close to the Coulomb barrier. The core mechanism involves the formation of a dinuclear system (DNS) resembling a molecule under the influence of nuclear forces between the projectile and target nuclei. The DNS formed in the collision may evolve along two distinct pathways. One is the formation of a compound nucleus, which subsequently de-excites by emitting light particles and γ-rays or through fission (fusion-fission, FF). Alternatively, in contrast to forming a compound nucleus, the DNS may undergo quasi-fission, which can be regarded as an MNT process, where extensive nucleon exchange takes place. within an extremely short time. Experimental and theoretical studies on the synthesis of heavy nuclei via MNT reactions date back to the 1970s [17−27]. To date, several laboratories, such as JINR, LBNL, Orsay, GSI, and IMP, have discovered numerous isotopes via MNT reactions [28−32]. These theoretical and experimental results provide multi-faceted and multi-level tools for understanding and predicting reaction processes.

Research on MNT reactions primarily focuses on two major nuclear regions that remain insufficiently explored: The first is the neutron-rich superheavy region, where theoretical predictions suggest new spherical shell closures near proton numbers Z = 114,120, or 126 and neutron number N = 184, forming the so-called "island of stability" [33−37]. Such nuclides cannot be synthesized via conventional fusion-evaporation reactions, and MNT reactions, particularly in very heavy systems, offer a feasible pathway for their production. The second is the neutron-rich region below lead, where nuclides closely associated with the astrophysical r-process are typically produced through fragmentation or fission reactions. Notably, both experiments and theory indicate that in this region, the cross-sections of MNT reactions can even exceed those of fragmentation reactions, with the yield advantage becoming more pronounced as the neutron number of the product increases and the proton number decreases [38−43].

In this paper, we report experiments in the ^{48}Ca− and ^{54}Cr−induced reactions with ^{238}U and ^{243}Am targets, which were performed at Spectrometer for Heavy Atoms and Nuclear Structure-2 (SHANS2) at CAFE2 [44]. The recoils detected in the experiment were primarily attributed to QF reactions. In the offline analysis, recoil nuclei with atomic numbers in the range of $84 \le Z \le 90$ were identified via the position-time-energy correlation method, and their production yields and implantation energies were determined. By comparing the distributions and yields of MNT products, we probe their dependence on the reaction, thereby providing useful information for future studies on MNT reactions. Additionally, several fission events were observed that could not be attributed to the decay chains of SHNs. This study provides valuable insights for ongoing SHN synthesis experiments at SHANS2 and serves as a reference for corresponding theoretical studies.

II. EXPERIMENT

The experiments (^{54}Cr +^{243}Am, ^{48}Ca +^{243}Am and ^{54}Cr +^{238}U) were conducted at the CAFE2 facility. Ion beams were generated by an electron cyclotron resonance ion source (ECRIS) and accelerated to energies near the respective Coulomb barriers by a superconducting linear accelerator.

For the ^{54}Cr +^{243}Am experiment, the beam energy was 7 MeV above the Coulomb barrier for the reaction system [45]. The beam intensity was maintained at approximately 0.60 pμA, resulting in a total integrated dose of 2.27×10^{18} particles. The ^{243}Am material was electrochemically deposited onto 2-μm-thick titanium foil to fabricate four arc-shaped targets with a thickness of 48 μg/cm^2. These targets (with the target backings facing the beams) were uniformly distributed along the perimeter of a 10-cm-diameter rotating target wheel, which maintained a rotational speed of approximately 2900 rpm during irradiation.

In the ^{48}Ca +^{243}Am experiment, americium targets were prepared analogous to those described previously, with an average thickness of 556 μg/cm^2. The ^{48}Ca^{14+} ion beam was accelerated to 256 MeV (an energy of 6 MeV above the Coulomb barrier) with a typical intensity of 0.55 pμA [45].

For the ^{54}Cr +^{238}U experiment, we employed ten arc-shaped targets consisting of ^{238}U (470 μg/cm^2) electrochemically deposited on 2.2-μm-thick titanium backings. These targets were mounted on a 20-cm-diameter rotating target wheel operating at 1500 r/min during irradiation. The ^{54}Cr^{17+} ion beam was accelerated to 310 MeV, which is 9 MeV above the Coulomb barrier of the system,

with a typical intensity of 2.0 pμA [45]. The operational parameters of all experiments are listed in Table 1.

The reaction products were recoiled from the target and transported into a separator filled with helium gas at a pressure of 100 Pa. This system has been demonstrated to achieve high transmission efficiency and considerable suppression of primary beam particles. After separation, recoils were implanted into a 300-μm-thick double-sided silicon strip detector (DSSD, BB17, Micron Semiconductor Ltd), which features 48 horizontal strips and 128 vertical strips, with an effective area of 48 mm×128 mm. Six single-sided silicon strip detectors (SSDs) surround the DSSD, each with a thickness of 500 μm and an effective area of 120 mm×63 mm, for the detection of α-particles and fission fragments escaping from the DSSD. The overall detection system achieved an efficiency of 86% for detecting α particles released in nuclear decay events. To differentiate between decay events and implanted events, two multi-wire proportional chambers (MWPCs) are placed at distances of 28 cm and 37 cm before the DSSD and filled with isobutane gas at a pressure of 300 Pa. Additionally, three square 300-μm-thick silicon detectors, each with an effective area of 50 mm×50 mm, are installed in parallel behind the DSSD to reject particles that penetrate the DSSD. The signals from all detectors are amplified by preamplifiers and subsequently digitized by a digitizer (V1724, CAEN S.p.A.), which operates at a sampling rate of 100 MHz. The energy resolution for α particles detected by the DSSD is approximately 30 keV (FWHM). For escaping α particles, the energy can be reconstructed by summing the energy deposits in both the DSSD and surrounding SSDs, resulting in a reconstructed energy resolution of ≈80 keV (FWHM). Further details regarding the SHANS2 system and detection apparatus can be found in Ref. [44].

III. RESULTS

In these experiments, the α-decay chains of various nuclides were identified using the position-energy-time correlation method. Figures 1(a), (c), (e) display the DSSD energy spectra for all events recorded in the ^{48}Ca +^{243} Am, ^{54}Cr +^{243} Am, and ^{54}Cr +^{238} U reactions, respectively. The black solid line represents the spectrum of all events recorded by the DSSD. The red solid line corresponds to the spectrum obtained from the DSSD in anti-coincidence only with the MWPCs. The green solid line corresponds to the spectrum obtained from the DSSD in anti-coincidence only with the Veto detector. The blue solid line corresponds to the spectrum obtained from the DSSD under the simultaneous anti-coincidence requirement with both the MWPCs and Veto detector. Figures 1(b), (d), (f) show the spectra of all events within the 6 − 20 MeV region from Figs. 1(a), (c), (e), respectively, revealing several distinct α-particle peaks. The energy range of 16 − 19 MeV primarily corresponds to decay events as pile-up signals. A pulse fitting technique was employed to process the digital α-decay signals of short-lived nuclei in the present experiments [46]. The minimum time separation achievable with our extraction method is approximately 120 ns.

Furthermore, as shown by the green curve in Figs. 1(a), (c), (e), spectral peaks are observed in the 60–100 MeV and 190–220 MeV regions. The former originates from the high-energy implantation of transfer reaction products, which is analyzed below, while the latter arises from scattered beam particles. The blue curve shows the spectrum of events recorded by the DSSD under the simultaneous anti-coincidence requirement with both the MWPCs and Veto detector, which has a similar event distribution to the green curve within the energy range of 60−220 MeV. Owing to the sub-100% detection efficiency of MWPC, a small portion of the implantation events were not registered.

To ensure accurate analysis of most nuclides, the correlation time window was determined by the half-lives of the nuclides and the average detector count rates measured in the experiments. The counting rates of the implantation events ($E > 1$ MeV) at the whole DSSD were 8.4 Hz (^{48}Ca+^{243}Am), 29.8 Hz (^{54}Cr+^{243}Am), and 24.2 Hz (^{54}Cr+^{238}U) at the typical beam intensities listed in Table 1. The α-particle energy spectra correlated with recoil implantation (RI) for all three experiments, which were acquired with a search time window of $120\ \text{ns} < \Delta t(RI - \alpha_1) < 100\ \text{s}$, are presented in Fig. 2. By comparing the experimentally measured half-lives and α-particle energies with literature data, we identified nuclides exhibiting high statistics, which are labeled. It can be observed that the peaks with high statistics in the one-dimensional energy spectrum are all due to the overlap of

Table 1. Summary of the measurements: target thickness, Coulomb barrier energy in the frame of laboratory calculated in [45], energy of the beam E_{lab}, beam energy at the center of target E_{cot}, typical beam intensity, and beam dose. Note that the ^{243}Am and ^{238}U targets were electrically deposited on titanium backings with thicknesses of 2 and 2.2 μm, respectively.

Reaction	Target thickness/(μg·cm^{-2})	Coulomb barrier energy/MeV	E_{lab}/MeV	E_{cot}/MeV	Beam intensity/pμA	Beam dose/ions
^{54}Cr +^{243}Am	448	288	314	295	0.60	2.27×10^{18}
^{48}Ca +^{243}Am	556	236	256	242	0.55	8.88×10^{17}
^{54}Cr +^{238}U	470	281	310	290	2.0	2.24×10^{19}

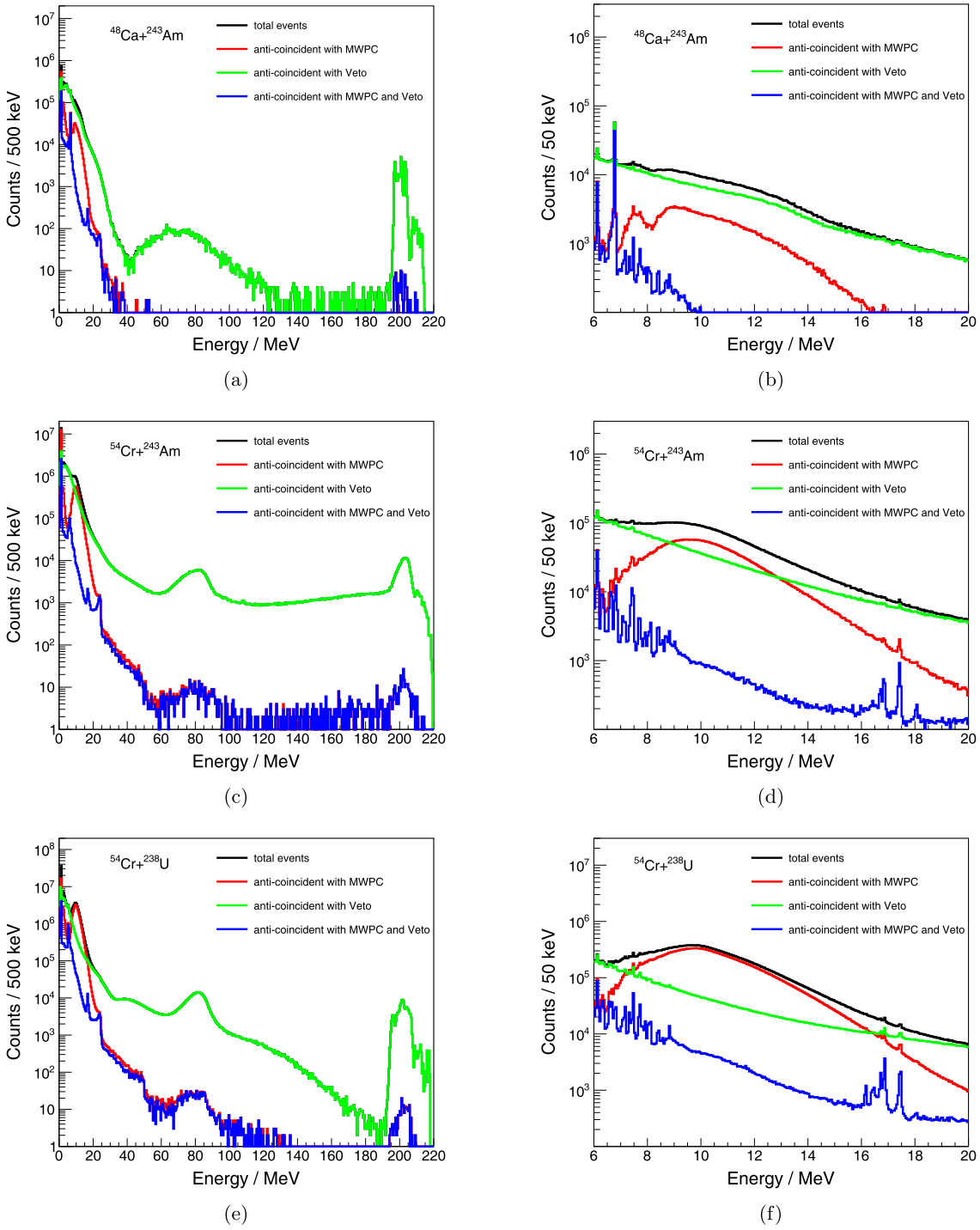

Fig. 1. (color online) DSSD energy spectra from the ^{48}Ca +^{243}Am (a), ^{54}Cr +^{243}Am, (c) and ^{54}Cr +^{238}U (e) experiments. The black solid line represents the energy spectrum of all events recorded by the DSSD. The red solid line corresponds to the spectrum of events recorded by the DSSD in anti-coincidence only with the MWPCs. The green solid line corresponds to the spectrum of events recorded by the DSSD in anti-coincidence only with the Veto detector. The blue solid line corresponds to the spectrum of events recorded by the DSSD under the simultaneous anti-coincidence requirement with both the MWPCs and Veto detector. (a), (c), (e) display the energy range from 0 to 220 MeV. (b), (d), (f) detail the 6−20 MeV energy range.

multiple nuclides. These peaks correspond to (^{219}Rn, ^{246}Cf), (^{242}Cm), (^{220}Ra, ^{221}Ac, ^{211}Po, ^{215}Po), (^{223}Ac, ^{221}Ra, ^{222}Ra, ^{220}Fr, ^{219}Rn), (^{219}Fr, ^{223}Th), (^{218}Fr, ^{219}Ra, ^{221}Ac, ^{214}Po), (^{212}At, ^{218}Fr, ^{220}Ac), (^{216}Rn, ^{215}At), (^{218}Rn, ^{224}Th), (^{220}Rn, ^{221}Fr), and (^{217}At, ^{222}Ac). Among these, ^{242}Cm and ^{246}Cf, marked in red, were residues from a previous ^{48}Ca

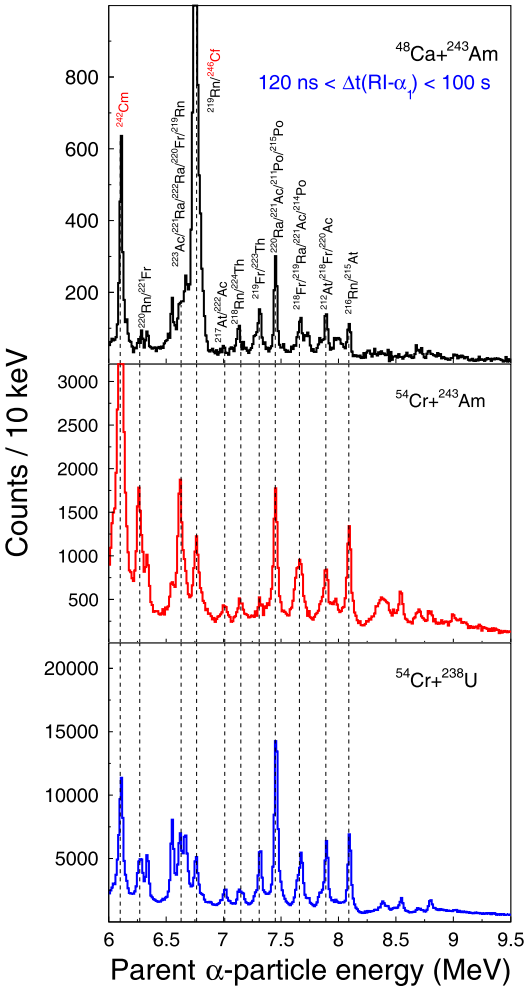

Fig. 2. (color online) Energy spectra of α particles correlated with their RI signals within a 100−120 s window in the ^{48}Ca +^{243}Am, ^{54}Cr +^{243}Am, and ^{54}Cr +^{238}U experiments.

+^{208}Pb experiment conducted with this apparatus. Owing to their long half-lives, they persist on the DSSD and are not products of the present experiments. The one-dimensional energy spectra from the three experiments exhibit similarities, indicating consistent nuclide production.

Nuclides produced in the experiments were further identified via RI-α_1-α_2 correlations. Figure 3 presents the two-dimensional energy spectrum of correlated parent and daughter α particles. The search time windows were $120\ \text{ns} < \Delta t(RI-\alpha_1) < 100\ \text{s}$ and $120\ \text{ns} < \Delta t(\alpha_1-\alpha_2) < 1\ \text{s}$. These conditions were determined based on the performance of our detection system and the half-lives of the nuclides identified within the region.

In Fig. 4, the E_{RI} distributions for ^{219}Ra, ^{220}Ra, and ^{221}Ra from the ^{54}Cr +^{243}Am reaction are presented. The E_{RI} distributions are resolved into distinct high-energy (HEC) and low-energy (LEC) components. A combined analysis of the TASCA results [47] and previous similar analyses from SHANS2 [48] reveals that the produced nuclides exhibit a bimodal distribution in implantation

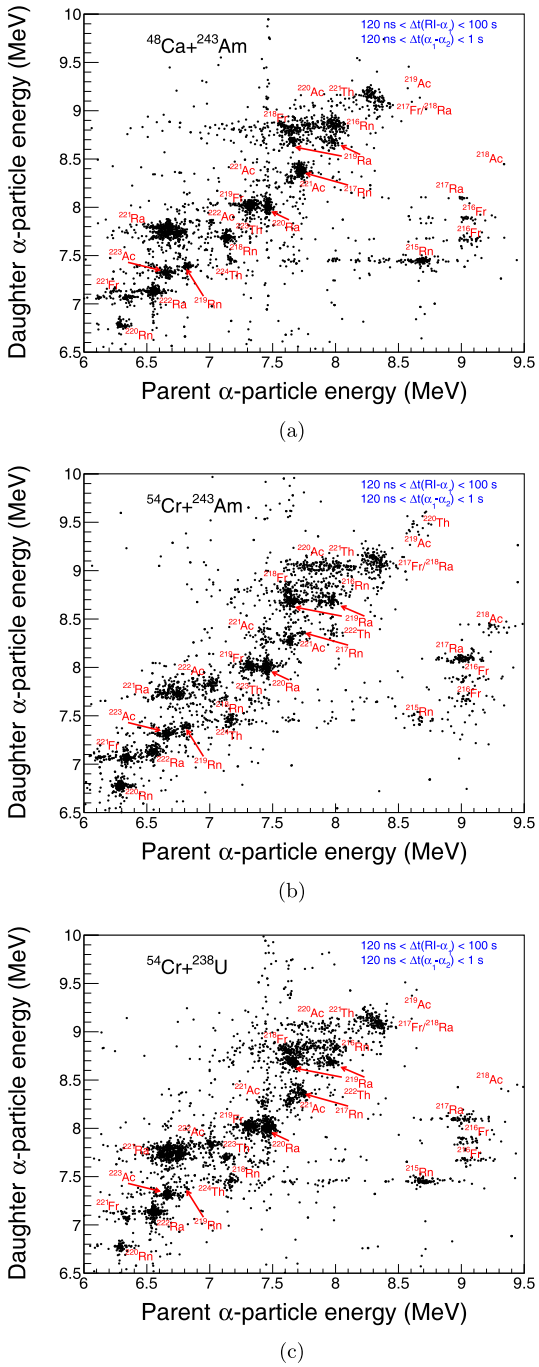

Fig. 3. (color online) Two-dimensional energy spectrum from the RI-α_1-α_2 correlation under the RI-α_1 and α_1-α_2 search time windows of 120 ns - 100 s and 120 ns - 1 s for the ^{48}Ca+^{243}Am (a), ^{54}Cr+^{243}Am (b), and ^{54}Cr+^{238}U (c) experiments. For the different reactions, the beam dose was maintained at a comparable level of approximately 5×10^{17} particles to achieve clear graphical representation of the data.

energy (HEC/LEC), which appears to be linked to the reaction mechanism. Figure 5 shows the recoil energy loss ΔE of implanted nuclei in the MWPCs as a function of E_{RI} for ^{220}Ra in the ^{54}Cr +^{243}Am experiment. The energy

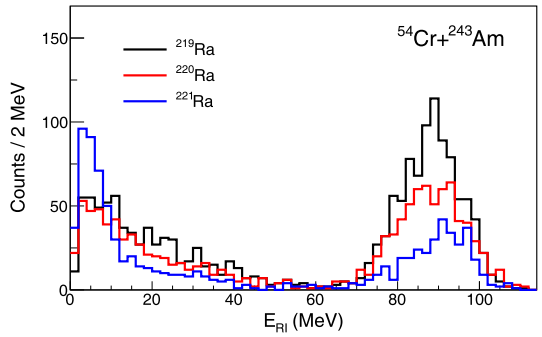

Fig. 4. (color online) Implantation energy distributions of Ra isotopes in the DSSD detectors for the ^{54}Cr +^{243}Am experiment.

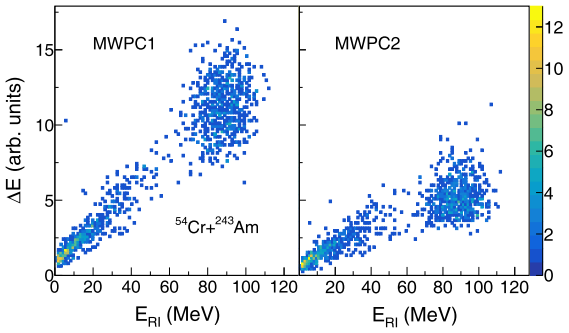

Fig. 5. (color online) Energy losses of ^{220}Ra in MWPC1 and MWPC2 as a function of recoil energy in the ^{54}Cr +^{243}Am experiment.

loss of ^{220}Ra in either MWPC1 or MWPC2 is distinctly divided into two components, corresponding to the LEC and HEC. The HEC also correlates with the peak in the 60−100 MeV energy region of the green curve in Figs. 1(a), (c), (e). The LEC spectrum exhibits a low-energy tail. Events below 1 MeV are excluded. Figure 6 presents the time distributions of the *RI*-α correlations for ^{220}Ra events belonging to the HEC and LEC. The time distributions for these two components show no significant difference and are consistent with the half-life value of ^{220}Ra ($T_{1/2}$ = 18(2) ms [49]).

Accurate determination of the yield of each nuclide in this nuclear region presents difficulties due to the significant overlap in α-decay energies and half-lives for some nuclides. For instance, it is impossible to distinguish between directly implanted ^{218}Ra (8383(4) keV, 25.91(14) μs [50]) and ^{217}Fr (8313(5) keV, 22(5) μs [51]) isotopes. Furthermore, some nuclides have extremely short lifetimes and decay almost instantly. To analyze the production yield of individual nuclides in these experiments, consistent identification criteria were applied across the three runs. Due to uncertainties in the transport efficiency ϵ of transfer reaction products for SHANS2, the cross section σ for each nuclide could not be determined. Consequently, the relative yield $\sigma\epsilon$ was presented in Table 2. The deduced α-particle energies and

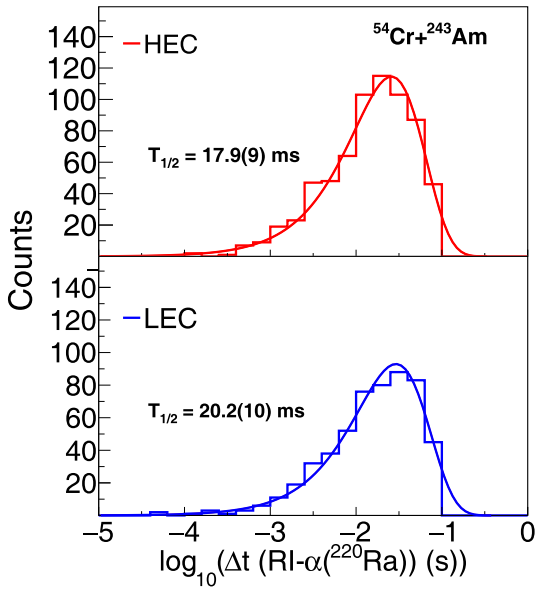

Fig. 6. (color online) Time distribution of ^{220}Ra produced in the ^{54}Cr +^{243}Am reaction, with HEC and LEC recoils represented by solid red and solid blue lines, respectively.

half-lives for all nuclides identified with *RI*-α_1-α_2 correlations in the three experiments was listed in Table 2, along with comparisons to literature reference values. For longer-lived nuclei (half-lives on the order of minutes), the measured half-lives in these experiments were generally do not match literature values, as noted in the table. This was due to the high probability of random correlation, which prevents an accurate determination of the temporal correlation between implanted nuclei and α-particles. Some nuclei exhibit multiple α-decay energies that are too close to be resolved. For nuclei that either do not exhibit *RI*-α_1-α_2 correlation or have excessively long half-lives, reliable relative yields cannot be determined. Consequently, Table 2 does not include all nuclides identified in these experiments.

The presence of fission-like events in the experiments was inferred from the analysis of the energy spectrum. The selection required a coincidence between the DSSD and SSD signals and a deposited energy in the DSSD of greater than 80 MeV. To suppress background events, a threshold of 2 MeV was applied to the SSD. The fission candidates identified in all three experiments are presented in Fig. 7. Four, eight, and two fission-like events were observed in the ^{48}Ca+^{243}Am, ^{54}Cr+^{243}Am, and ^{54}Cr+^{238}U reactions, respectively. Detailed characteristics of these events are provided in Table 3. The lifetimes of these events are predominantly distributed in the millisecond range. All observed events can be tentatively attributed to the fission of implanted nuclei, likely short-lived fission isomers near the target (*e.g.*, ^{243m}Am and ^{242m}Am), as in Refs. [31, 61].

Table 2. α-decay characteristics of transfer-reaction products are presented for each reaction. Columns 2−4 report relative yields derived from experiments ^{48}Ca+^{243}Am,^{54}Cr+^{243}Am, and ^{54}Cr+^{238}U, respectively. Columns 5 and 6 detail the α-particle energies and half-lives experimentally determined for these isotopes. Corresponding reference values from the literature are provided in Columns 7 and 8. The solid lines (—) indicate nuclei with half-lives longer than 1 min, which cannot be determined accurately. Owing to the high implantation rate, the probability that these nuclei are correlated with a random implantation event exceeds 80% [52]. An asterisk (*) in the upper-right corner indicates corrections applied to the relative yields for very short-lived nuclei (or for those whose daughter nuclei have very short half-lives).

Isotopes	^{48}Ca+^{243}Am	^{54}Cr +^{243}Am	^{54}Cr +^{238} U	This work		Literature data		Ref.
	$\sigma\epsilon$/pb	$\sigma\epsilon$/pb	$\sigma\epsilon$/pb	E_α/keV	$T_{1/2}$	E_α/keV	$T_{1/2}$	
^{221}Th	1(1)	16(2)	6(2)	8129(14),8447(15)	1.47(30) ms	8143(3),8469(4)	1.75(3) ms	[53]
^{222}Th		37(3)	14(3)	7978(9)	1.81(24) ms	7982(2)	1.964(2) ms	[54]
^{223}Th	6(3)	54(4)	48(6)	7329(9)	0.60(5) s	7298(7),7286(10),7323(5)	0.60(2) s	[55]
^{224}Th	18(5)	98(6)	100(8)	6999(10),7164(10)	0.88(4) s	7000(10),7170(10)	1.05(2) s	[49]
^{218}Ac	1(1)*	36(3)*	10(3)*	9247(18)	1.58(26) μs	9213(10)	1.03(5) μs	[50]
^{219}Ac	10(3)*	131(6)*	39(5)*	8629(16)	15.9(17) μs	8664(10)	11.8(15) μs	[56]
^{220}Ac	29(6)*	328(10)*	166(11)*	7821(11)	22.8(9) ms	7855,7709,7792,7652,7670	26.4(2) ms	[57]
^{221}Ac	34(6)	368(11)	288(14)	7637(11),7430(10)	43.9(11) ms	7642(4),7437(4)	52(2) ms	[53]
^{222}Ac	28(6)	192(8)	245(13)	7008(9)	5.7(3) s	7008.6(20)	4.9(5) s	[54]
^{223}Ac	163(14)	317(10)	517(19)	6658(7),6570(9)	—	6646.7(10),6661.6(10), 6563.7(10)	2.10(5) min	[55]
^{217}Ra	14(4)	169(7)	113(9)	9012(17)	1.75(9) μs	8992(8)	1.6(2) μs	[51]
^{219}Ra	107(11)	510(13)	560(20)	7654(11),7966(11)	10.2(3) ms	7678(3),7988(3)	10(3) ms	[58]
^{220}Ra	191(15)	388(11)	667(21)	7457(9)	17.9(5) ms	7453(7)	18(2) ms	[57]
^{221}Ra	227(16)	283(10)	658(21)	6615(8),6750(7), 6677(8)	22.9(8) s	6607,6754,6662	28(2) s	[53]
^{222}Ra	239(17)	241(9)	608(20)	6553(7)	26.9(5) s	6558(5)	33.6(4) s	[54]
^{216}Fr	34(6)*	80(5)*	111(9)*	9026(17)	0.91(6) μs	9004(5)	0.70(2) μs	[59]
^{218}Fr	126(12)*	127(6)*	278(14)*	7618(11),7690(11)	20.2(7) ms	7616(4),7681(4),7657(5)	21.9(5) ms	[50]
^{219}Fr	314(19)	146(7)	494(18)	7314(9)	27.4(12) ms	7312(2)	20(2) ms	[56]
^{220}Fr	232(17)	67(5)	335(15)	6674(7),6609(7)	25.8(12) s	6677(4),6633(4)	27.4(3) s	[57]
^{221}Fr	245(17)	828(16)	294(14)	6338(5),6117(5)	—	6341(13),6126.3(15)	4.801(6) min	[53]
^{215}Rn	154(14)	72(5)	214(12)	8687(15)	2.7(12) μs	8674(8)	2.30(10) μs	[60]
^{216}Rn	185(15)*	55(4)*	213(12)*	8000(13)	64(4) μs	8050(10)	45(5) μs	[59]
^{217}Rn	170(14)	40(4)	190(11)	7711(11)	0.62(3) ms	7738(3)	0.59(6) ms	[51]
^{218}Rn	185(15)	22(3)	136(10)	7133(9)	32.4(16) ms	7129(2)	33.75(15) ms	[50]
^{219}Rn	139(13)	217(8)	114(9)	6817(7),6559(8)	5.76(34) s	6819.1(3),6552.6(10)	3.96(1) s	[56]
^{220}Rn	91(10)	439(12)	209(12)	6287(5)	—	6288.1(1)	55.6(1) s	[57]

IV. DISCUSSION

In these three reactions targeting the superheavy region, we identified 58 isotopes originating from MNT reactions using identical data analysis procedures, of which 52 were directly implanted into the DSSD. As shown in Fig. 8, all identified nuclides populate the region northeast of ^{208}Pb (spanning N =126−136 and A=210−226), reflecting the influence of the doubly magic ^{208}Pb core. The nuclide distributions from the three experiments exhibit no significant differences, showing almost complete overlap. This result is consistent with findings from the ^{50}Ti +^{249}Cf experiment performed at TASCA [47].

The relative yields ($\sigma\epsilon$) for Th, Ac, Ra, Fr, and Rn in each experiment are displayed in Fig. 9. The $\sigma\epsilon$ values for the various isotopes exhibit a consistent correlation with mass number across the three experiments, with Ra, Fr, and Rn isotopes exhibiting higher relative yields. For in-

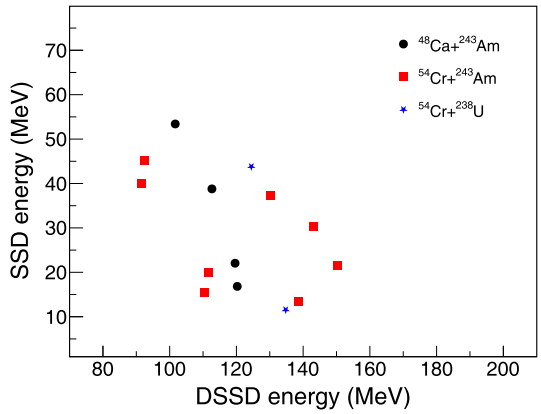

Fig. 7. (color online) Fission-like events in the ^{48}Ca+^{243}Am, ^{54}Cr+^{243}Am and ^{54}Cr+^{238}U experiments. Events were selected by requiring a coincident trigger between the DSSD and SSD, with energy thresholds of 80 MeV in the DSSD and 2 MeV in the SSD, and an anti-coincident condition with the MWPCs and Vetos.

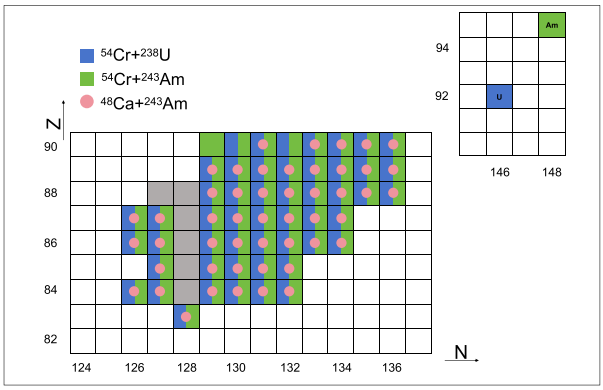

Fig. 8. (color online) Isotopic distributions identified using the energy-position-time correlation method produced in the experiments involving ^{48}Ca +^{243}Am (pink dots), ^{54}Cr +^{243}Am (green), and ^{54}Cr +^{238}U (blue). Gray shading denotes nuclides originating from the decay of implanted nuclei, rather than from direct implantation into the DSSD.

stance, a general decrease in relative yield is observed with an increasing number of transferred neutrons (from the target region towards ^{208}Pb), consistent with the findings reported in Ref. [30]. The maxima of the isotopic distributions for MNT products are found at neutron-to-proton ratios N/Z close to that of the entrance-channel system [30]. The N/Z ratios for the reactions shown in Fig. 9 are 1.530, 1.517, and 1.496, respectively. For Th isotopes, the relative yield maxima occur at approximately A = 227, 226, and 224. Isotopes with mass numbers up to 224 were observed in all reactions, leading to an increase in relative yields with increasing A, although their relative yields remain significantly lower than those of other nuclides. For Rn isotopes, the relative yield maxima are located at approximately A = 217, 216, and 214. Consequently, Rn isotopes exhibit flatter relative yield distributions in the ^{48}Ca+^{243}Am and ^{54}Cr+^{238}U reactions. For isotopes of Fr–Ac elements, the relative yield dependence is intermediate between those of Rn and Th. When comparing these different reactions, it is found that

Table 3. Details of all observed fission events for each experiment, including the spatial distributions within the DSSD and SSD detectors and the corresponding energy depositions. All events result from fission processes initiated by direct nuclear implantation. The probability of observing random correlation with RI-fission events forming a decay chain was estimated to be 2.4×10^{-6}, 9.5×10^{-6}, and 1.8×10^{-5} in ^{48}Ca+^{243}Am, ^{54}Cr+^{243}Am and ^{54}Cr+^{238}U, respectively [52].

Reaction	DSSD-XPos	DSSD-YPos	SSD Pos	Implantation energy /MeV	DSSD energy /MeV	SSD energy /MeV	Total energy /MeV	Lifetime
^{48}Ca +^{243}Am	97	36	17	2.62	119.60	22.04	141.64	39.02 μs
	10	43	27	7.25	101.66	53.40	155.06	10.65 ms
	45	44	43	12.98	120.25	16.83	137.08	73.77 ms
	122	6	40	11.16	112.66	38.79	151.45	33.68 ms
^{54}Cr +^{243}Am	75	44	4	11.57	142.86	30.36	173.22	3.08 ms
	13	23	15	19.46	110.17	15.31	125.48	0.15 ms
	106	35	41	11.32	138.33	13.41	151.74	2.00 ms
	120	44	40	3.93	91.53	39.91	131.44	0.55 ms
	25	25	25	8.64	150.04	21.39	171.43	2.10 ms
	6	13	33	5.77	111.35	19.90	131.25	2.15 ms
	86	16	32	2.76	92.26	45.11	137.37	1.67 ms
	43	9	21	7.32	129.89	36.84	166.73	14.68 ms
^{54}Cr +^{238}U	34	16	25	3.62	124.47	43.80	168.27	1.38 ms
	82	30	11	19.65	134.77	11.55	146.32	0.58 ms

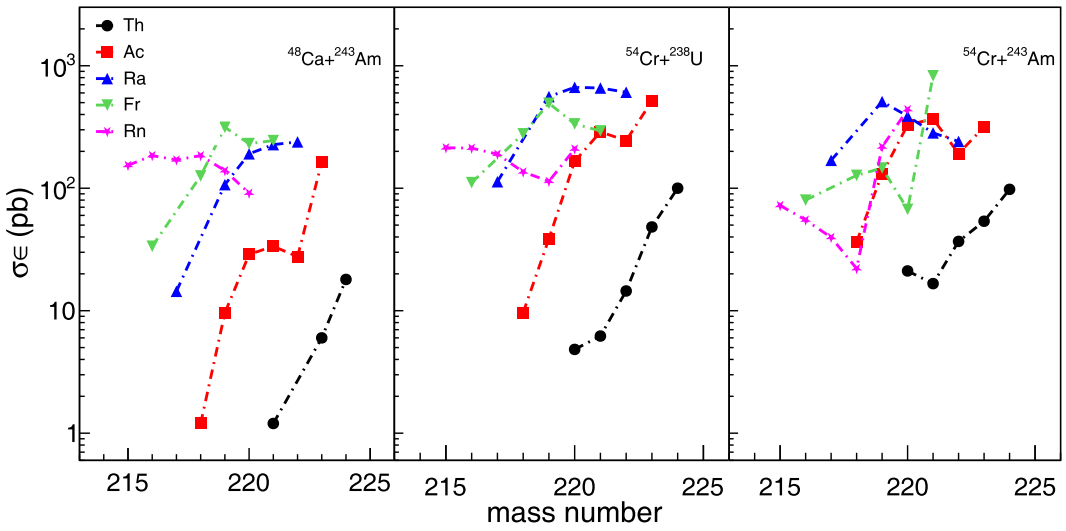

Fig. 9. (color online) Relative yields ($\sigma\epsilon$) of implanted Th, Ac, Ra, Fr, and Ra isotopes as a function of mass number (A), which were produced in the ^{48}Ca+^{243}Am, ^{54}Cr+^{243}Am, and ^{54}Cr+^{238}U experiments. Here, σ represents the cross-section and ϵ denotes the efficiency.

the relative yields of the nuclides generally show a monotonic increasing trend through the ^{48}Ca+^{243}Am, ^{54}Cr+^{238}U, and ^{54}Cr +^{243}Am reactions.

In these experiments, the MNT cross-sections are notably higher than those of fusion-evaporation, suggesting that the projectile-target interaction lasts sufficiently long to form a DNS, which subsequently fractures within an extremely short time. The observed distribution of all MNT nuclides migrating from the target region toward ^{208}Pb indicates that the DNS decays into two splits with considerable mass asymmetry. The heavier fragment corresponds to the detected nuclides, and the lighter one remains unidentified. We suggest that the identified isotopes may originate from QF processes, owing to the influence of the doubly magic ^{208}Pb [47, 48]. The fragmentation process involves the emission of fragments at random angles relative to the beam direction. Light fragments emitted along the beam direction result in heavier fragments exhibiting LEC characteristics, whereas emission opposite to the beam direction leads to the HEC effect [22, 47, 62].

It is conceivable that quasi-elastic scattering products may be produced in these reactions. However, these products, typically remaining in the vicinity of the target and characterized by either long half-lives or decay via β-emission, cannot be identified by our detection system. Furthermore, we cannot distinguish between quasi-fission and deep inelastic scattering processes with the current settings.

V. SUMMARY

The study of ^{48}Ca+^{243}Am, ^{54}Cr+^{243}Am, and ^{54}Cr+^{238}U reactions was conducted in CAFE2 using SHANS2. Analysis reveals that, despite variations in individual nuclide yields across different reactions, their dependence on the number of transferred nucleons exhibits a consistent trend, indicating distinct systematic patterns of product distributions in these reactions. Furthermore, we suggest that the identified isotopes may originate from QF processes. However, experimental data on this reaction mechanism remain scarce. These findings impose significant constraints on theoretical models describing the dynamics of QF in heavy-ion collisions, thereby helping to clarify unresolved aspects of different reaction mechanisms and providing new perspectives for understanding their underlying features.

ACKNOWLEDGMENTS

The authors would like to express their thanks to the ion-source group and the accelerator crew of CAFE2 for providing the stable ^{54}Cr and ^{48}Ca beams.

References

[1] W. D. Myers and W. J. Swiatecki, Nucl. Phys. **81**, 1 (1966)
[2] Y. T. Oganessian and V. K. Utyonkov, Rep. Prog. Phys. **78**, 036301 (2015)
[3] S. Hofmann, D. Ackermann, S. Antalic *et al.*, Eur. Phys. J. A **32**, 251 (2007)
[4] L. Stavsetra, K. E. Gregorich, J. Dvorak *et al.*, Phys. Rev. Lett. **103**, 132502 (2009)
[5] C. E. Düllmann, M. Schädel, A. Yakushev *et al.*, Phys. Rev. Lett. **104**, 252701 (2010)
[6] P. A. Ellison, K. E. Gregorich, J. S. Berryman *et al.*, Phys. Rev. Lett. **105**, 182701 (2010)
[7] D. Rudolph, U. Forsberg, P. Golubev *et al.*, Phys. Rev. Lett.

111, 112502 (2013)
[8] J. Khuyagbaatar, A. Yakushev, C. E. Düllmann *et al.*, Phys. Rev. Lett. **112**, 172501 (2014)
[9] J. M. Gates, G. K. Pang, J. L. Pore *et al.*, Phys. Rev. Lett. **121**, 222501 (2018)
[10] C. E. Düllmann, R. D. Herzberg, W. Nazarewicz, and Y. Oganessian, Nucl. Phys. A **944**, 1 (2015)
[11] S. A. Giuliani, Z. Matheson, W. Nazarewicz *et al.*, Rev. Mod. Phys. **91**, 011001 (2019)
[12] Z. Wang and Z. Ren, Eur. Phys. J. A **60**, 74 (2024)
[13] A. Såmark Roth, D. M. Cox, D. Rudolph *et al.*, Phys. Rev. Lett. **126**, 032503 (2021)
[14] V. I. Zagrebaev and W. Greiner, Phys. Rev. C **83**, 044618 (2011)
[15] V. Saiko and A. Karpov, Eur. Phys. J. A **58**, 41 (2022)
[16] G. G. Adamian, N. V. Antonenko, A. Diaz. Torres *et al.*, Eur. Phys. J. A **56**, 47 (2020)
[17] D. N. Poenaru and R. A. Gherghescu, EPL **124**, 52001 (2018)
[18] M. Schädel, W. Brüchle, H. Gäggeler *et al.*, Phys. Rev. Lett. **48**, 852 (1982)
[19] H. Freiesleben, K. D. Hildenbrand, F. P. hlhofer *et al.*, Z. Phys. A **292**, 171 (1979)
[20] A. Türler, H. R. von Gunten, J. D. Leyba *et al.*, Phys. Rev. C **46**, 1364 (1992)
[21] E. M. Kozulin, G. N. Knyazheva, K. V. Novikov *et al.*, Phys. Rev. C **94**, 054613 (2016)
[22] J. Tōke, R. Bock, G. Dai *et al.*, Nucl. Phys. A **440**, 327 (1985)
[23] M. Itkis, A. Bogachev, I. Itkis *et al.*, Nucl. Phys. A **787**, 150 (2007)
[24] I. M. Itkis, E. M. Kozulin, M. G. Itkis *et al.*, Phys. Rev. C **83**, 064613 (2011)
[25] R. du Rietz, E. Williams, D. J. Hinde *et al.*, Phys. Rev. C **88**, 054618 (2013)
[26] G. Giardina, G. Mandaglio, A. Nasirov *et al.*, Nucl. Phys. A **970**, 169 (2018)
[27] H. Gäggeler, W. Brüchle, M. Brügger *et al.*, Phys. Rev. C **33**, 1983 (1986)
[28] S. Heinz and H. M. Devaraja, Eur. Phys. J. A **58**, 114 (2022)
[29] M. Thoennessen, *The Discovery of Isotopes, A Complete Compilation* (Cham, Switzerland: Springer International Publishing, 2016)
[30] H. Devaraja, A. Yeremin, M. Chelnokov *et al.*, Phys. Lett. B **862**, 139353 (2025)
[31] S. Heinz, H. M. Devaraja, O. Beliuskina *et al.*, Eur. Phys. J. A **52**, 278 (2016)
[32] Z. G. Gan, W. X. Huang, Z. Y. Zhang, X. H. Zhou, and H. S. Xu, Eur. Phys. J. A **58**, 158 (2022)
[33] R. Smolánczuk, J. Skalski, and A. Sobiczewski, Phys. Rev. C **52**, 1871 (1995)
[34] M. Bender, K. Rutz, P. G. Reinhard *et al.*, Phys. Rev. C **60**, 034304 (1999)
[35] M. Bender, Phys. Rev. C **61**, 031302 (2000)
[36] S. Ćwiok, W. Nazarewicz, and P. H. Heenen, Phys. Rev. Lett. **83**, 1108 (1999)
[37] S. Cwiok, P. H. Heenen, and W. Nazarewicz, Nature **433**, 705 (2005)
[38] G. G. Adamian, N. V. Antonenko, and W. Scheid, Phys. Rev. C **68**, 034601 (2003)
[39] G. G. Adamian, N. V. Antonenko, and A. S. Zubov, Phys. Rev. C **71**, 034603 (2005)
[40] G. G. Adamian, N. V. Antonenko, V. V. Sargsyan *et al.*, Phys. Rev. C **81**, 057602 (2010)
[41] N. Wang, Z. Li, and X. Wu, Phys. Rev. C **65**, 064608 (2002)
[42] C. Li, J. Tian, and F.-S. Zhang, Phys. Lett. B **809**, 135697 (2020)
[43] Z. Feng, Phys. Rev. C **95**, 024615 (2017)
[44] S. Xu, Z. Zhang, Z. Gan *et al.*, Nucl. Instrum. Methods Phys. Res. A **1050**, 168113 (2023)
[45] N. Wang, Chin. Phys. C **49**, 124106 (2025)
[46] H. B. Yang, Z. G. Gan, Z. Y. Zhang *et al.*, Eur. Phys. J. A **55**, 8 (2019)
[47] A. Di Nitto, J. Khuyagbaatar, D. Ackermann *et al.*, Phys. Lett. B **784**, 199 (2018)
[48] F. Guan, Z. Zhang, H. Zhou *et al.*, Chin. Phys. C **49**, 074004 (2025)
[49] E. Browne and J. Tuli, Nucl. Data Sheets **112**, 1115 (2011)
[50] S. Zhu and E. McCutchan, Nucl. Data Sheets **175**, 1 (2021)
[51] M. Basunia, Nucl. Data Sheets **181**, 475 (2022)
[52] K. H. Schmidt, C. C. Sahm, K. Pielenz *et al.*, Z. Phys. A **316**, 19 (1984)
[53] F. Kondev, E. McCutchan, B. Singh *et al.*, Nucl. Data Sheets **147**, 382 (2018)
[54] B. Singh, M. Basunia, M. Martin *et al.*, Nucl. Data Sheets **160**, 405 (2019)
[55] B. Singh, G. Mukherjee, S. Basu *et al.*, Nucl. Data Sheets **175**, 150 (2021)
[56] A. K. Kar, S. K. Choudhary, and V. K. Singh, J. Clean. Prod. **376**, 134120 (2022)
[57] S. C. Wu, Nucl. Data Sheets **108**, 1057 (2007)
[58] B. Singh, G. Mukherjee, D. Abriola *et al.*, Nucl. Data Sheets **114**, 2023 (2013)
[59] K. Auranen and E. McCutchan, Nucl. Data Sheets **168**, 117 (2020)
[60] B. Singh, D. Abriola, C. Baglin *et al.*, Nucl. Data Sheets **114**, 661 (2013)
[61] Y. T. Oganessian, V. K. Utyonkov, D. Ibadullayev *et al.*, Phys. Rev. C **106**, 024612 (2022)
[62] B. M. Kayumov, O. K. Ganiev, A. K. Nasirov *et al.*, Phys. Rev. C **105**, 014618 (2022)